



Cite this: *React. Chem. Eng.*, 2025, 10, 2311

## Unraveling the role of ultrasound in hydrothermal interzeolite conversion using a tubular ultrasound-integrated reactor†

Elena Brozzi, <sup>a</sup> Michiel Dusselier <sup>b</sup> and Simon Kuhn <sup>\*a</sup>

In the past years, ultrasound has been considered a sustainable process intensification technique for zeolite synthesis. However, understanding the link between ultrasound phenomena and their related effects has remained a challenge due to the limited availability of hydrothermal ultrasonic reactors and parameter standardization among the studies. In this work, a novel ultrasound-integrated tubular coiled reactor is presented, which enables fast and efficient ultrasonic hydrothermal zeolite synthesis. Specifically, the effect of ultrasound irradiation and its underlying mechanisms on high silica FAU-to-MFI interzeolite conversion is studied. Unseeded syntheses in the presence of an organic structure-directing agent (OSDA) are performed at 160 °C for residence times up to 2 h. The presence of hydroxyl radicals generated by ultrasound is assessed *via* terephthalic acid dosimetry at different temperatures and pressures as a measurement of the cavitation activity. The application of 20 W ml<sup>-1</sup> of suspension reveals an enhanced MFI growth rate and faster crystallization completion, resulting in an overall increase in the mean crystal size. Ultrasound is also successful in counteracting solid deposition on the walls of the coiled reactor. Applying hydrothermal conditions to this setup suppresses radical formation, indicating very weak transient cavitation activity. Therefore, these observations are attributed to the enhanced mass transfer *via* ultrasonic wave propagation, which renders the dissolved material more readily available for crystal growth.

Received 3rd April 2025,  
Accepted 25th June 2025

DOI: 10.1039/d5re00149h  
[rsc.li/reaction-engineering](http://rsc.li/reaction-engineering)

## 1 Introduction

For more than 20 years, ultrasound (US) has risen as a promising external energy input for enhanced zeolite nucleation and growth.<sup>1–3</sup> As a whole, ultrasound is an established process intensification technology widely applied during the synthesis of solid materials.<sup>4</sup> Zeolite processing is most commonly associated with the application of low-frequency ultrasound (20–100 kHz), where acoustic cavitation and wave propagation are the main occurring phenomena. Acoustic cavitation describes the formation, growth, oscillation, and possible collapse of gas bubbles in a sonicated liquid. The bubble behaviour depends on the ultrasonic frequency and power, as well as liquid temperature and pressure.<sup>5,6</sup> The cavitation bubble collapse creates local high temperature and pressure regions, which can give rise to transport phenomena-related effects, and additionally can

homolytically split solvent molecules, thereby forming radicals (chemical effects). Wave propagation refers to mechanical sinusoidal oscillations which cause fluctuations in fluid pressure, density, and particle velocity and position.<sup>4</sup> In the presence of solid matter, such as zeolite crystals, the cavitation bubble collapse becomes asymmetrical and forms liquid jets, increasing shear forces and molecular collisions, also resulting in fragmentation, de-agglomeration, and surface erosion.<sup>4</sup> The strength with which acoustic cavitation and wave propagation can impact zeolite crystallization is also dependent on several system parameters, such as reactor geometry, initial solution viscosity, density and surface tension, and also solid particle size and concentration.<sup>7–9</sup>

Ultrasound was first applied to zeolite crystallization during the pretreatment of the precursor gel to obtain highly crystalline, narrowly distributed zeolites.<sup>10</sup> Park *et al.* used it for the first time during the synthesis of zeolite 4A from kaolin, while a couple of years later Andaç and coworkers were the first ones to perform ultrasonic synthesis of zeolite A from synthetic sources.<sup>11,12</sup> Since then, ultrasound has been applied during zeolite synthesis starting from several waste sources, such as coal fly ash, rice husk ash, industrial waste, or natural sources.<sup>13–16</sup> In contrast, the use of ultrasound during zeolite synthesis from purified chemical sources has been reported by a limited number of publications, especially

<sup>a</sup>Department of Chemical Engineering, KU Leuven, Celestijnenlaan 200F, 3001 Leuven, Belgium. E-mail: simon.kuhn@kuleuven.be

<sup>b</sup>Center for Sustainable Catalysis and Engineering, KU Leuven, Celestijnenlaan 200F, 3001 Leuven, Belgium

† Electronic supplementary information (ESI) available. See DOI: <https://doi.org/10.1039/d5re00149h>



**Table 1** Available studies in the literature that apply ultrasound (US) during synthesis, conditions and main observations compared to non-irradiated synthesis. CSD = crystal size distribution

Ref.	Zeolite type	Temperature and synthesis time	US settings and probe	Comparison to silent synthesis
Andaç <i>et al.</i> <sup>12</sup>	A (LTA)	50–60 °C, up to 15 h	Bath, unknown	Higher yield Larger crystal size
Gürbüz <i>et al.</i> <sup>21</sup>	S-1 (MFI)	75 °C, up to 82 h	Bath, 300–600 W	Higher crystal number density Same yield and crystallinity in shorter time
Pal <i>et al.</i> <sup>20</sup>	NaP (GIS)	Up to 80 °C, 3 h	Bath, 150 W	Formation of crystalline phase after 3 h without thermal treatment
Tadjarodi <i>et al.</i> <sup>23</sup>	Y (FAU)	90 °C, 3 h	Horn, 150 W	3 h for synthesis completion No precise info on size and yield
Ramirez Mendoza <i>et al.</i> <sup>22</sup>	X (FAU)	80 °C, up to 3 h	Transducer, 0.3 W mL <sup>-1</sup>	20% faster crystallization Higher mass transfer, hot spots
Chen <i>et al.</i> <sup>17</sup>	ZSM-5 (MFI)	80 °C, up to 145 h	Horn, 323 W	Similar final yield
Dewes <i>et al.</i> <sup>18</sup>	A (LTA)	80 °C, up to 4 h	Horn, 0.25 W cm <sup>-3</sup>	CSD dependent on power No info on yield More uniform CSD
Nzodom Djozing <i>et al.</i> <sup>19</sup>	A (LTA)	80–100 °C, up to 4 h	Horn, 19 W	Transformation to sodalite Smaller crystallite size

if compared to its use during pre- or post-treatment steps. Table 1 summarises these studies with their main findings.<sup>12,17–23</sup>

All studies report a faster crystallization rate of the target zeolite. Some of them highlight a final smaller mean crystal size under ultrasonic conditions compared to the silent case,<sup>17,18</sup> while others a similar or even larger final size.<sup>12,21</sup> Sonication time plays a major role in the effects observed on the final products: prolonged sonication can cause a decrease in crystallinity,<sup>20</sup> or even a phase change.<sup>19</sup> Higher sonication power is usually related to an enhanced nucleation rate, which is attributed to the formation of radicals from cavitation bubble collapse,<sup>17,20</sup> to the presence of hotspots and increased mass transfer,<sup>22</sup> or to the sonofragmentation of the viscous hydrogel, which promotes the formation of smaller nuclei.<sup>19</sup> Lower sonication power is linked with growth-related effects instead.<sup>17</sup> Furthermore, as all the aforementioned studies differ among themselves in solution viscosity (e.g., clear solution, hydrogel, sol-gel), reactor size, applied ultrasonic power and device – which highly affect the strength of the ultrasonic phenomena<sup>24</sup> – it still remains challenging to link the observed effects and the applied process conditions with the underlying ultrasound mechanism.

To address the viscosity issue often present in traditional hydrothermal synthesis from soluble sources, interzeolite conversion (IZC, also called interzeolite transformation) has emerged as an alternative, promising technique.<sup>1,25,26</sup> IZC benefits from the use of crystalline materials as (major) Si and Al sources, which transform into the target zeolite following favourable kinetic paths.<sup>25,27,28</sup> This translates, among other advantages, to faster and more selective crystallization and to the synthesis of new structures or of zeolites free from organic templates.<sup>26,29–32</sup>

However, IZC often requires higher temperatures (120–180 °C),<sup>29,33,34</sup> while US-assisted zeolite syntheses have

only been performed at temperatures of 100 °C at most.<sup>19</sup> The few available ultrasonic hydrothermal reactors, which can reach temperatures up to 200–220 °C,<sup>35–39</sup> have never been used for zeolite synthesis under such conditions. These setups couple a single ultrasound source with an autoclave-like configuration, therefore they would only partially overcome (thanks to the ultrasound) the limitations of traditional hydrothermal zeolite batch synthesis.<sup>40</sup> Moreover, very few studies give an insight into the sonochemical activity happening at elevated temperatures and pressures.<sup>39,41</sup> Most of the studies listed in Table 1 operate with small volume reactors, often ending up with a mismatch between the system adopted for US-assisted synthesis (ultrasonic bath in most cases) and the silent control experiments (conventional autoclaves in large ovens).

There is therefore a pressing need to design efficient US-integrated hydrothermal reactors for high-temperature zeolite synthesis, with the objective of enabling reliable setup characterization and direct comparison. These reactor-based efforts fit in the growing body of literature surrounding non-conventional zeolite synthesis methods.<sup>1,42–45</sup>

In this study, a novel tubular US-integrated reactor setup is used to perform FAU-to-MFI IZC, which enables direct comparison between irradiated and silent experiments. The reactor was previously characterized for its acoustic pressure field distribution and its ability to work with suspensions.<sup>46</sup> Herein, the setup is updated to withstand hydrothermal conditions and further characterized for the presence of ·OH radicals as an indication of transient cavitation activity. Afterwards, ultrasound is applied for the first time under hydrothermal conditions to IZC. The US-related effects on the transformation of FAU to MFI are studied, and a hypothesis of the potential ultrasonic mechanism to enhance crystallization is proposed.



## 2 Interzeolite conversion in different reactor setups

The following molar composition is used in all zeolite syntheses:  $1 \text{ SiO}_2 : \frac{1}{385} \text{ AlO}_2^- : 0.35 \text{ OSDA}^+ : 0.08 \text{ Na}^+ : 0.43 \text{ OH}^- : 20 \text{ H}_2\text{O}$ . All chemicals were used without further purification. The organic structure-directing agent (OSDA) used in all syntheses is tetrapropylammonium hydroxide (TPAOH, 40 wt%, Sigma Aldrich and SACHEM). FAU HSZ-390-HUA zeolite (2% water content, TOSOH Corp.) is used as the sole Si and Al source, with a Si/Al ratio of 385 according to the 'Certificate of Analysis' and ICP measurements. Sodium hydroxide (NaOH, 50 wt%) was purchased from Sigma Aldrich. 2.2 g of FAU385 is used to prepare each time fresh reactant suspension, which has a visual aspect of a milky liquid, with water-like viscosity at all stages during the preparation, as well as product collection.

The syntheses are performed under similar process conditions (160 °C, autogenous or applied pressure), in different reactor setups, in order to benchmark the US-integrated reactor performance with two other available systems: a traditional autoclave and a U-shaped tubular reactor. These three reactors differ in geometry, total volume, material, and heating method. The reactors are sketched in Fig. S3,† and their main similarities and differences are listed in Table S1.†

### 2.1 Autoclave synthesis

Traditional hydrothermal synthesis is carried out first in a Teflon-lined stainless steel autoclave. The liquid reagents (TPAOH, NaOH and Milli-Q water) are poured directly in the liner. After a short mixing time, FAU is added. The synthesis mixture is stirred at 500 rpm for about 10 min prior to closing the autoclave lid. The synthesis is carried out under stirring at 600 rpm in a convection oven preheated at 160 °C for different residence times between 30 and 120 min. After reaction, the autoclaves are cooled in a water bath for at least one hour. Eventually, the product is collected in a 50 mL tube, separated from the liquid and washed *via* centrifugation (8 min, 10 000 rpm) until reaching a final liquid pH < 9, and dried overnight in a static oven at 60 °C.

### 2.2 Tubular reactor synthesis

The reaction mixture is prepared in a 50 mL glass bottle by first mixing the OSDA, Milli-Q water, and NaOH, respectively. Afterwards, FAU is added, the suspension is briefly mixed and subsequently sonicated in an ultrasonic bath (VWR USC-THD, 45 kHz, 120 W) for 10 min at maximum power to de-agglomerate the larger FAU aggregates. Care is given that during sonication the temperature of the bath does not increase above 30 °C to avoid any possible premature aging of the mixture (see Fig. S1b† for more details). The suspension is kept under stirring and up to 4 reactors are loaded. The stainless steel U-shaped tubular reactors (TRs) are immersed at the same

time in a recirculating (1500 rpm) oil pump (Huber CC304) preheated at 160 °C temperature and taken out at different times according to the desired reaction time (between 10 and 120 min). The reactors are then cooled in an ice bath for 15 min prior to product collection. Centrifugation, washing, and drying follow the same procedure as described above.

### 2.3 Coiled reactor setup description and synthesis

The US-integrated hydrothermal reactor was initially characterized in a previous work,<sup>46</sup> but afterwards further adapted to withstand zeolite synthesis' harsh conditions. The coiled reactor (CR) is made of PTFE and has an internal diameter of 2 mm, with a thickness of 0.5 mm and length of 3.9 m, to reach a total volume of 12 mL. It is coiled around a custom 3D printed frame made with a high temperature resistant resin (High Temp V2 resin, Formlabs). The surrounding box is made of aluminium, with internal cavity dimensions of 150 mm × 40 mm × 40 mm (total cavity volume 240 mL). The internal reactor parts are depicted in the pink inset in Fig. 1. Ultrasound is delivered to the system by means of 6 Langevin-type transducers (Steminc) in a 2-1-2-1 symmetric configuration that optimizes the acoustic pressure field in the vicinity of the tubular reactor, and connected in parallel with each other.<sup>46</sup> The reactor operates at its resonance frequency of  $44 \pm 1 \text{ kHz}$  (at 160 °C and 6.5 bar) with an applied net power of  $240 \pm 5 \text{ W}$  and a voltage of  $1.25 \pm 0.5 \text{ Vpp}$  (power density of  $20 \text{ W mL}^{-1}$  considering the volume of the reacting solution, or  $1 \text{ W mL}^{-1}$  considering the entire cavity where the reactor is embedded). Fig. 1 shows the entire process section; all the lines are made of PFA tubing of  $1/8''$  diameter. A back pressure regulator (BPR, Swagelok) controls the pressure during the start-up and shutdown phase of the synthesis. Temperature is controlled by connecting the reactor box to a recirculating heating oil pump (Huber Ministat 230) used in external recirculation mode at 4500 rpm. The start-up of the system is done by delivering water *via* a HPLC pump (Instrument Solutions) until the desired pressure and temperature inside the reactor are achieved. When ultrasound is applied from the beginning of the experiment, an ultrasonic generator (DG1032Z Waveform Generator, Rigol technologies) and amplifier (E&I 1040L RF Power Amplifier) are turned on during this start-up phase to ensure system stability under hydrothermal conditions. Meanwhile, the reaction mixture is prepared following the procedure for the TR synthesis. The suspension is afterwards loaded into a 100 mL high-pressure syringe pump (Chemix) and delivered in a one-through injection, after which two ball valves are closed at the inlet and at the outlet of the reactor to ensure that the synthesis mixture remains inside. Inline temperature reading is performed inside the reactor box with a K-type thermocouple connected to a thermologger to record the temperature values during the synthesis. Fig. S4† shows the



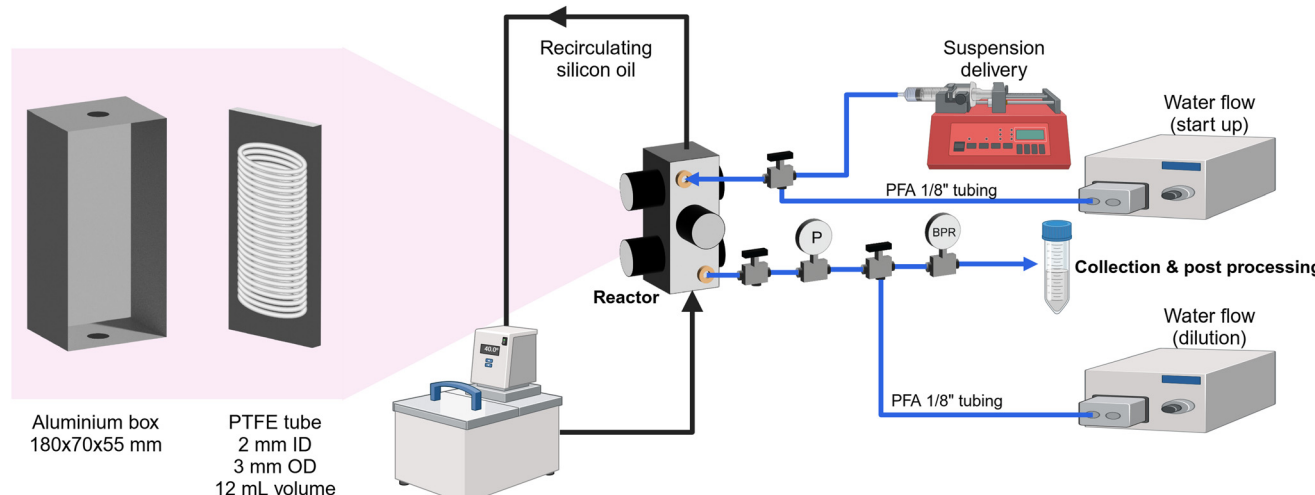


Fig. 1 Schematics of the reactor system designed for this work. Created with <https://Biorender.com>.

temperature profiles inside the recirculating pump and inside the box for the silent and sonicated cases. After reaction, the product solution is flushed out with the syringe used for delivery loaded with Milli-Q water. A total volume of 45 mL of product solution and water is collected in a 50 mL centrifuge tube and further processed as described above. After cooling, the reactor is cleaned according to the following procedure: first, the remaining water from the syringe is flushed through. Afterwards, ethanol (EtOH, absolute  $\geq 99.8\%$ , Fisher Chemical) is pumped *via* the HPLC pump in priming mode for a minimum of 3 reactor volumes, while ultrasound with a power above 200 W is applied to detach any possible deposits in the channel. For deposition studies in this work, the cleaning water and EtOH are collected and further processed as described above. Eventually, a 3 wt% KOH (powder, Sigma Aldrich) solution is pumped through the system *via* the HPLC pump for the final cleaning. In this system, silent as well as irradiated experiments can be performed in a reproducible manner, thanks to the ability to withstand hydrothermal conditions, and thanks to the independent bulk temperature and pressure control.

#### 2.4 Yield and crystallinity in the three different reactor setups

The evolution of the solid yield over time in the CR (Fig. 2) is benchmarked with the other reactors: the U-shaped TR and the Teflon-lined autoclave. Thanks to the better heat transfer and the reactor geometry, both the TR and the CR outperform the autoclave in terms of zeolite crystallization kinetics and solid yield.<sup>40,42,47</sup> The induction time in the TR and in the CR decreases to below 10 min, while in the autoclave reactor around 30 min are needed before the appearance of the first crystalline phase. TR kinetics is the fastest, likely due to

the higher heat conductivity and the small solution volume compared to the large heating reservoir used. Nevertheless, when applying ultrasound to the synthesis in the CR setup, the yield curve approaches that of the TR. Table S2<sup>†</sup> shows a statistically relevant difference between the average yield achieved in the CR in ultrasonic *vs.* silent mode for 20 and 30 min reaction time, while this gap ceases to be significant from 45 min reaction time onwards.

The solid yield is calculated accounting for the complete removal of  $\text{TPA}^+$  ions (see eqn S1 in Section S(II) in the ESI<sup>†</sup>), which is a reasonable approximation for all synthesis times  $\geq 20$  min, as shown by the TGA curves in Fig. S6a.<sup>†</sup> In the case of 20 min synthesis, faster  $\text{TPA}^+$  incorporation in the framework under ultrasonication is observed (Fig. S6b<sup>†</sup>). As a consequence, the incorporation of Si in the MFI framework is facilitated, showing a higher Si/Al ratio in the earlier stages of the synthesis (Fig. S7<sup>†</sup>).

From the PXRD patterns in Fig. 3, two different crystallization behaviours can be distinguished, which influence the yield evaluation as well: in the case of TR

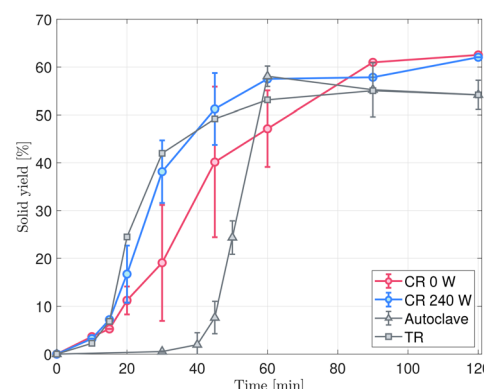


Fig. 2 Comparison of the net solid yield among different reactor systems.



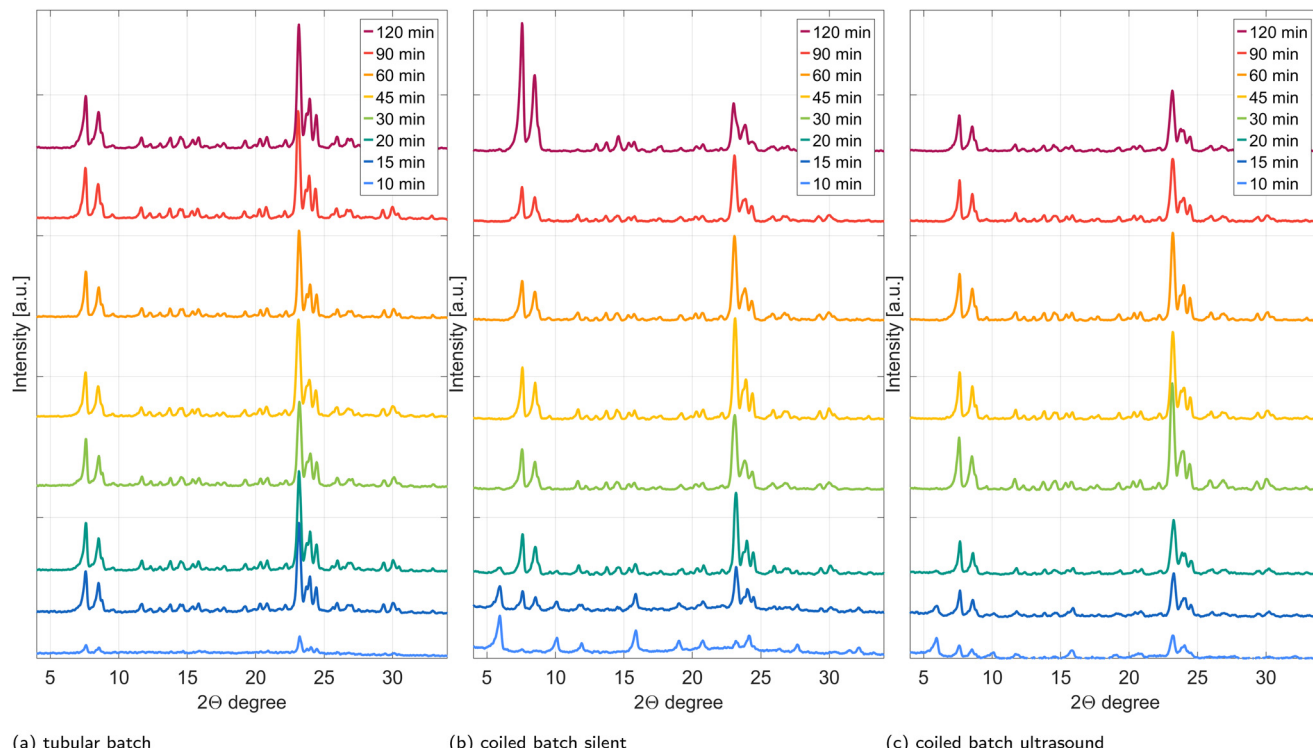


Fig. 3 PXRD pattern evolution between 10 and 120 min in different reactor systems.

synthesis (Fig. 3a), a full dissolution of the FAU takes place. Already after 10 min of synthesis, MFI peaks clearly appear and immediately grow to high crystallinity, reaching synthesis completion around 45–60 min. On the other hand, in the CR, the intermediate amorphization step is absent; MFI starts crystallizing while FAU is still dissolving. When comparing Fig. 3b and c with each other and with the reference patterns in Fig. S1a,† the long-range order of the FAU crystals (clearly visible around  $\theta = 6^\circ$ ) disappears only after 30 min of synthesis, but in the case of ultrasonic synthesis, the main MFI peaks around  $\theta = 23^\circ$  show up already within 10 min of synthesis and slowly grow more intense, while in the silent case MFI is detectable only after 15 min. Remainders of FAU within the first minutes of silent synthesis are hypothesized to be the cause for a high partial pressure tailing in  $N_2$  physisorption curves (Fig. S8†), as they look similar to the isotherm of the mother zeolite. Nevertheless, after the first appearance of the MFI peaks in Fig. 3b, crystallinity increases further, but the yield of the silent synthesis still lags behind almost until completion. This delay is well caught by the analysis of the first derivative of the yield curve (Fig. S9b†), where the maximum for the silent synthesis is reached only at 40 min compared to the US-assisted synthesis that peaks already around 22 min and reaches the end of the crystallization process after 60 min. It is therefore hypothesized that in the irradiated system, the species in the liquid phase are more readily available to promote the crystallization of the daughter zeolite.

### 3 Ultrasound-driven mechanisms and effects on FAU-to-MFI IZC

In this section, a specific focus is given first to understanding whether any cavitation activity takes place during hydrothermal US-assisted IZC. Afterwards, a link between experimental observations and potential ultrasound phenomena is made.

#### 3.1 Reactor characterization: detection of radicals *via* terephthalic acid dosimetry

Several studies report the benefit of introducing  $\cdot OH$  radicals during zeolite synthesis *via* a radical initiator or external radiation.<sup>17,20,48,49</sup> As the formation of radicals as a consequence of ultrasonic irradiation is an indicator of transient cavitation, it is of great interest to understand whether the US-integrated reactor is capable of producing  $\cdot OH$  radicals under hydrothermal conditions. Terephthalic acid (TA) dosimetry is an established technique in sonochemistry<sup>50–52</sup> as well as in other fields<sup>53–55</sup> for the detection of hydroxyl radicals. The reaction between TA and  $\cdot OH$  radicals produces 2-hydroxyterephthalic acid (2-HTA) with known conversion,<sup>56</sup> which can be easily evaluated *via* fluorescence spectroscopy. More details on the experimental procedure are given in Section S(III) in the ESI.† The results in Fig. 4a are displayed as the intensity of the fluorescence spectra of 2-HTA at different temperatures and pressures, relative to ambient temperature and pressure conditions (25



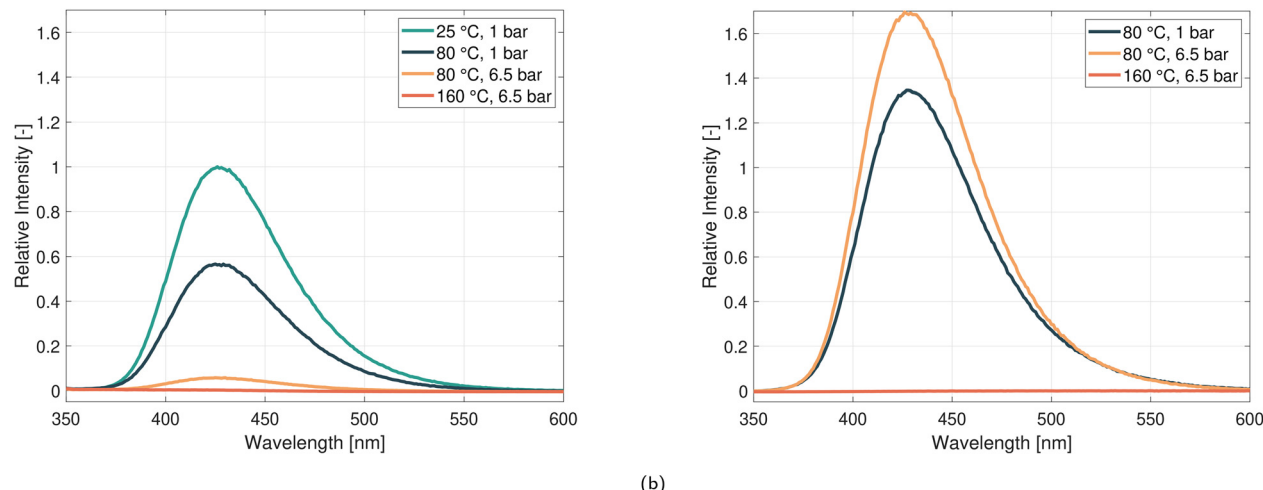


**Fig. 4** Fluorescence spectra of 2-hydroxyterephthalic acid as a consequence of the interaction between terephthalic acid and radicals produced in the CR under different process conditions *via* (a) ultrasonication and (b) sodium persulfate as a radical initiator. All the curves have been normalized based on the intensity of the curve obtained from ultrasound-generated radicals at 25 °C and 1 bar.

°C, 1 bar),<sup>52</sup> when applying ultrasound to form radicals. Increasing the temperature and the pressure of the system has a detrimental effect on the formation of radicals that are US-induced, as both the vapour pressure of the system and the threshold pressure to overcome for cavitation bubble collapse increase.<sup>57</sup> Under synthesis conditions (160 °C, 6.5 bar), no signal can be detected, hinting to either inability to produce radicals or failure of the characterization technique. As a direct comparison, dosimetry is performed with sodium persulfate (SPS) as a radical initiator. It is clear from Fig. 4b how, in this case, pressure is not a limiting factor for the production of radicals as it is for the case with ultrasound. Instead, it appears that pressurizing the system at 80 °C has a positive effect: the relative fluorescence intensity (as compared to the US-generated radicals curve at 25 °C and 1 bar) increases from 1.3 to 1.7 at 1 and 6.5 bar, respectively. Surprisingly, also in this case, no radicals can be detected

under IZC synthesis conditions. The HPLC chromatogram (in Fig. S10b†) on the liquid product obtained after dosimetry with SPS in hydrothermal conditions shows the presence of multiple peaks not belonging to either TA or 2-HTA. Interestingly, the HPLC chromatogram of the US-generated radical dosimetry solution (Fig. S10a†) shows only the presence of the TA peak. Therefore, this same solution was then recycled for another dosimetry experiment at 80 °C with SPS to check whether radical production could still occur. As shown in Fig. S11,† the reused solution successfully produced radicals, even though with a lower intensity. This suggests that for the ultrasound case, high temperatures and pressures do not affect the chemical structure of the compound but simply suppress high energy transient cavitation bubble collapse.<sup>57</sup> This proves that in the CR, under the applied synthesis conditions, ultrasound cannot generate ·OH radicals.

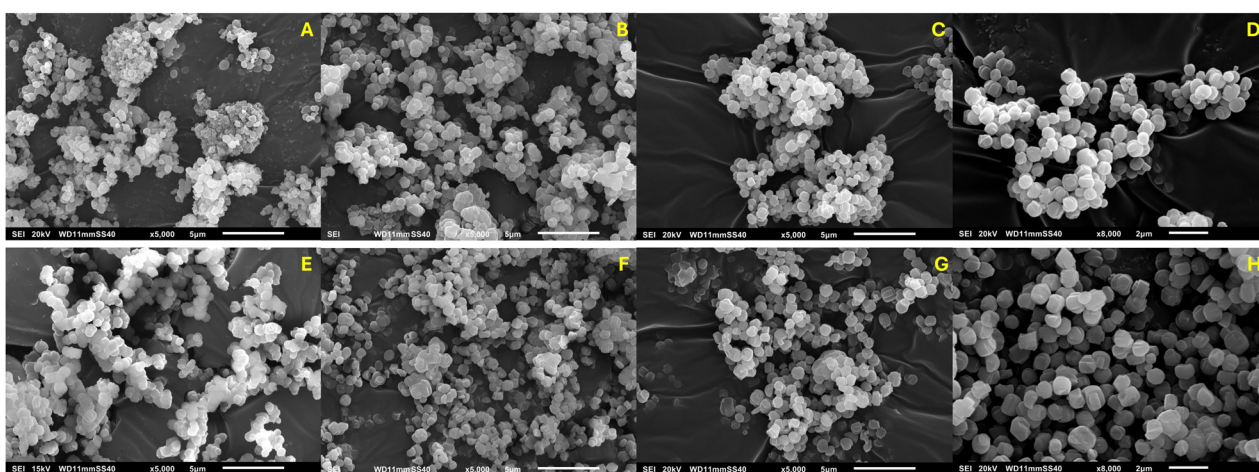


**Fig. 5** SEM images of MFI growth over time under silent conditions: (A) 30 min, (B) 45 min, (C) 60 min, (D) 120 min; and under ultrasonication: (E) 30 min, (F) 45 min, (G) 60 min, (H) 120 min.



Supplementary studies were performed by varying temperature and pressure to establish which process conditions enable radical formation and detection. As shown in Fig. S12a and b,<sup>†</sup> only temperatures  $\leq 90$  °C and input power  $\geq 240$  W (20 W mL<sup>-1</sup> of suspension) seem adequate to form a substantial amount of radicals. Several IZC experiments were therefore executed at 90 °C, which however could not confirm any active role of the ·OH radicals during the synthesis, despite their presence according to TA dosimetry. More information can be found in Section S(IV) in the ESI.<sup>†</sup>

### 3.2 Crystal size distribution and morphology

Fig. 5 contains selected SEM images that show the crystal size evolution of MFI zeolites and their morphology. All samples exhibit a pseudo-spherical shape, which evolves over time towards an octagonal-shaped morphology with twin intergrowth,<sup>58</sup> even though not very well defined, especially

in the first stages of silent synthesis (Fig. 5A and B). In line with the available literature,<sup>17,21</sup> the use of ultrasound does not seem to affect the morphology of the final MFI product. From Fig. 5A, it is possible to see some undissolved FAU clusters, (reference SEM image of FAU in Fig. S2<sup>†</sup>) with a crystal size of about 500 nm, while MFI starts from 500 to 700 nm and grows larger (Fig. 5B to D for silent synthesis and Fig. 5E to H for US-assisted synthesis). As the MFI crystal size appears to be always larger than that of the parent FAU, it can be hypothesized that the early formation of a few templated MFI nuclei serves as ‘seeds’ for further MFI nucleation at the FAU surface.<sup>29</sup>

Evaluation of the crystal size distribution (CSD) under silent and sonicated conditions in Fig. 6 reveals that already at 20 min the average size of the crystals is larger for irradiated samples. Under silent conditions, represented in Fig. 6a, the average crystal size after 20 and 30 min is similar, and the distribution presents a growing tail at 30 min. MFI shifts to larger sizes with a unimodal distribution until 45 min, but after that the crystals seem to stop growing and the distribution narrows, as also visible from the evolution of the mean size in Fig. S17a,<sup>†</sup> while the yield slightly increases until 60 min. On the other hand, the larger US-made MFI crystals keep growing until 60 min (Fig. S17b<sup>†</sup>), after which the size no longer changes. It is difficult to draw any conclusion from size and size distribution data compared at the same time points (‘vertically’ on the yield plot), as all these distributions reach different solid yield values at different times. Therefore, cross-comparison of the CSD ‘horizontally’, *i.e.* at the same yield values, is done (as symbolized in Fig. 7a). From left to right in Fig. 7b, CSD evolution comparison is made between 20 min US and 30 min silent (case A), 30 min US and 45 min silent (case B), 45 min US and 60 min silent (case C), and 120 min of both silent and US, *i.e.*, the end of the process (case D). In case A, after 20 min of sonication, the particles have grown larger as compared to 30 min without irradiation. It is hypothesized that the just-formed nuclei under ultrasound undergo preferential growth thanks to the higher availability of the material in solution. Thus, the nucleation stage likely ends earlier compared to the silent case, probably causing formation of fewer nuclei. These crystals are also detectable earlier under PXRD (Fig. 3c). This process causes presumably faster material depletion in solution. For this reason, in cases B and C, yield and size become similar between the compared curves, as under silent conditions the growth rate reaches its maximum (Fig. S17a<sup>†</sup>), to then drop soon after, just as quickly, and stops around 60 min upon reaching the steady state yield. Under ultrasonication, as most of the supersaturation was consumed within the first 30 min, the growth rate increases more slowly, peaking after about 40 min, but holds for a longer time, indicating a prolonged process duration (Fig. S17b<sup>†</sup>). Eventually, between 60 and 120 min (case D), MFI crystals under ultrasonication grow even larger until they reach a similar final yield as in the silent case, likely dictated by the same thermodynamic equilibrium.

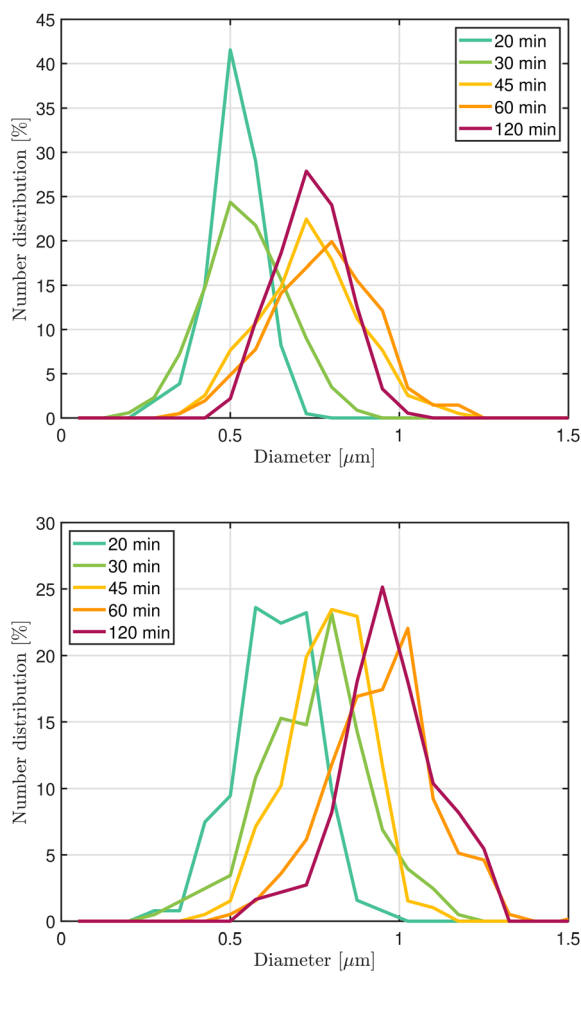
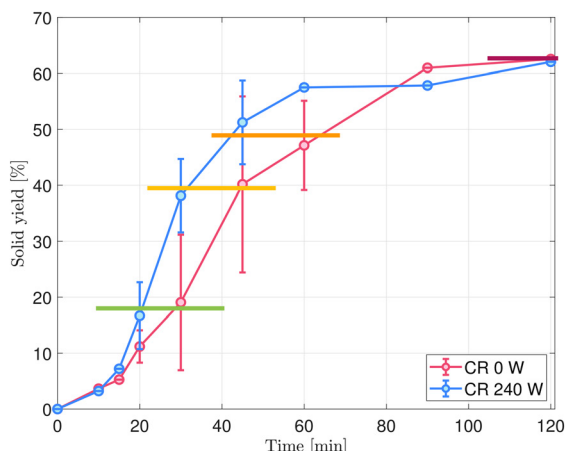
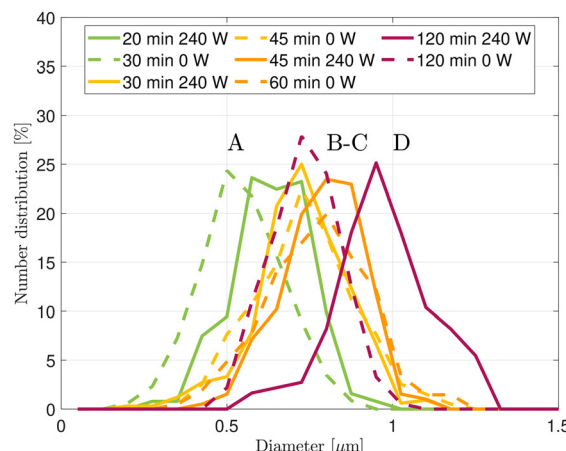


Fig. 6 Evolution of the number crystal size distribution over time for MFI synthesized (a) under silent conditions and (b) under ultrasonication. All the curves are created from a minimum of 300 particles.





(a)



(b)

**Fig. 7** (a) Net solid yield evolution over time for the CR without ultrasound (0 W) and under 240 W ultrasonication. The horizontal coloured lines highlight at which time points the comparison of the crystal size distribution (CSD) is performed, which is displayed in (b). For the evaluation of these CSDs, a minimum of 300 single particles are analysed.

The fact that probably fewer nuclei were formed, together with the enhanced mixing provided by wave propagation, enables further material incorporation. No major conclusions can be drawn on the nucleation stage, due to either the absence of transient cavitation or the fact that the already fast kinetics of this IZC system prevents further enhancement of the nucleation step.

### 3.3 Partial sonication and solid deposition evaluation

Partial sonication experiments are performed to focus the irradiation time either on the nucleation or on the growth stage of IZC. Ideally, application of ultrasound during the first minutes of the synthesis should mostly affect nucleation, while starting sonication at a later stage, once nucleation is completed, should impact the crystal growth. A

total of 30 min of residence time is chosen; here, ultrasound is applied only for a part of the experiment: at the beginning of the synthesis, for the first 10 or 20 min (out of the total 30 min), or at the end of the synthesis, again for either 20 or 10 min until completion of the 30 min. Care is taken that when switching the mode of operation, the temperature of the recirculating temperature control bath is adjusted to take into account the heat dissipation from ultrasound (see Fig. S5†). The dashed bars in Fig. 8 represent how much time out of those 30 min (full length of the bars) the solution is irradiated, and when. The right axis is related to the solid yield obtained at the end of each experiment, while the left axis shows the mean crystal size with the standard deviation. It is clear that stopping the irradiation before the end of the experiment (ON-OFF cases) does not improve the final yield collected compared to the fully silent case. However, when

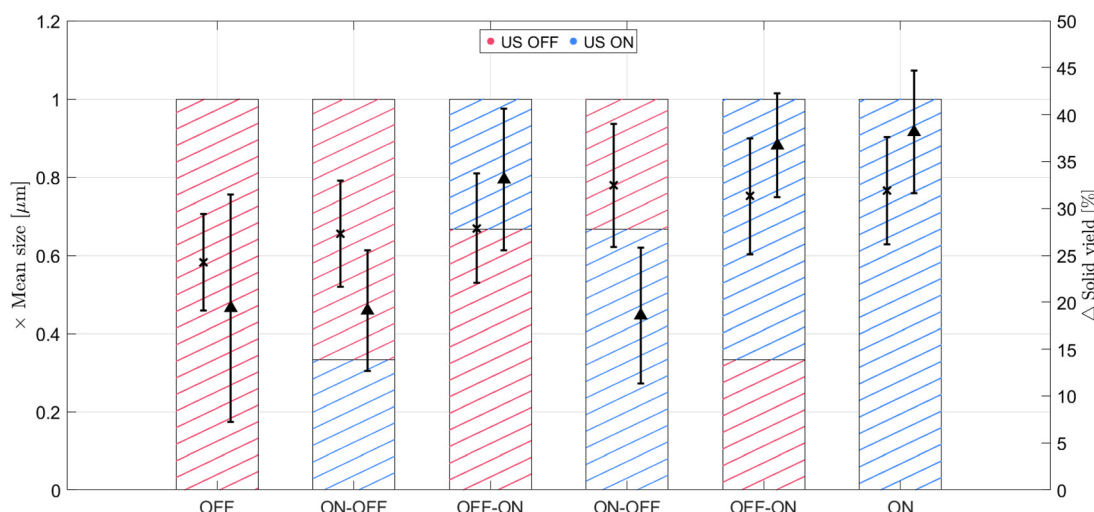


**Fig. 8** Solid yield ( $\Delta$ ) and mean crystal size ( $\times$ ) for partial sonication experiment when 240 W power ultrasound (US) is applied for either 10 or 20 min on a total reaction time of 30 min, represented by the total height of the bar, and the top of the bar represents the end of the experiment.



looking at the PXRD patterns in Fig. S18a,† irradiation in the first minutes of the synthesis shows a small but positive effect on FAU dissolution the longer ultrasound is applied to the system. When ultrasound is started during the experiments (at minute 10 or 20) and kept on until the end of the 30 min reaction time (OFF-ON cases), a steep rise in the total solid yield and the largest increase in crystallinity (Fig. 8 and S18b,† respectively) is obtained.

Interestingly, when 10 min of sonication is applied, the mean crystal size remains similar to the non-sonicated case, regardless of the sonication moment. This suggests that 10 min of sonication is not sufficient to provide substantial MFI growth enhancement or any visible effect on nucleation, but end-of-reaction sonication allows collection of all the solid material that tends to deposit in the reactor (see also Fig. S19a,†). Likewise, for  $\geq 20$  min irradiation, sonication in the second part of the reaction successfully counteracts solid deposition. However, larger crystal sizes are obtained regardless of the irradiation moment, showing a clear effect of ultrasound on crystal growth.

As 240 W power is proven capable of enhancing MFI crystal growth, ultrasonic synthesis is also performed at 120 W net power (10 W  $\text{mL}^{-1}$  of reactant suspension) for a 30 min reaction time. From Fig. S19a and b,† it can be concluded that also a power as low as 120 W is enough to prevent extensive solid deposition, observed when no ultrasound was used, but the growth rate is enhanced substantially only when 240 W net power is applied. Overall, it can be concluded that irradiating the solution for 20 min at 240 W out of 30 min reaction time, in the second part of the experiment, is enough to avoid deposition, and at the same time enhances the growth rate.

## 4 Conclusions

In this work, the effect of ultrasound on FAU-to-MFI interzeolite conversion is studied. A novel system is developed, consisting of a coiled tubular reactor embedded in an aluminium box where ultrasonic transducers are mounted, and silicon oil recirculates for temperature control. This tubular reactor design allows for enhanced mass and heat transfer compared to traditional batch autoclaves and can operate under silent and ultrasonic conditions, allowing for direct comparison between the two cases without relying on other types of reactors, which differ in geometry, heat transfer, and material properties. By irradiating the system, a substantial enhancement of the growth rate is achieved: it is hypothesized that once the nuclei form, they immediately start to grow larger instead of forming more nuclei, which explains the earlier detection of MFI peaks under PXRD, a larger mean crystal size and a shift of the crystal size distribution towards larger sizes compared to the silent case, but a similar final solid yield. Irradiating the suspension for 20 min or longer provides substantial MFI growth rate enhancement. A 99.5% increase in the average solid yield is obtained in 30

min synthesis time together with a 45.5% reduction of the standard deviation. This effect can be attributed to the increased mixing originating from ultrasonic wave propagation in the liquid, which makes the reacting material dissolved more readily available for crystal growth. Under IZC harsh temperature and pressure (160 °C, 6.5 bar), suppression of transient cavitation activity likely occurs, as no  $\cdot\text{OH}$  radicals forming from water splitting could be detected.

Besides the potential to affect zeolite crystallization kinetics, the use of ultrasound in the final minutes of synthesis, even when the power is reduced by 50%, successfully prevents particle deposition on the channel walls. This holds particular importance for zeolite synthesis where a solid-liquid system is formed, or is always present, as in the case of IZC starting with solid materials.

## Data availability

The data supporting this article have been included as part of the ESI,†

## Author contributions

E. B.: conceptualization, investigation, data curation, visualization, writing – original draft, writing – review & editing. M. D.: conceptualization, writing – review & editing, supervision. S. K.: conceptualization, data curation, writing – review & editing, supervision, funding acquisition.

## Conflicts of interest

There are no conflicts to declare.

## Acknowledgements

E. B. acknowledges FWO Flanders for a Strategic PhD fellowship (1S20025N). SACHEM is explicitly thanked for providing the organic structure-directing agent (TPAOH). M. D. thanks the European Research Council (ERC) for funding (ERC Starting Grant 948449 named Z-EURECA).

## References

- 1 A. Deneyer, Q. Ke, J. Devos and M. Dusselier, *Chem. Mater.*, 2020, **32**, 4884–4919.
- 2 E.-H. Yuan, R. Han, J.-Y. Deng, W. Zhou and A. Zhou, *ACS Appl. Mater. Interfaces*, 2024, **16**, 29521–29546.
- 3 S. Askari, S. Miar Alipour, R. Halladj and M. H. D. A. Farahani, *J. Porous Mater.*, 2013, **20**, 285–302.
- 4 C. Devos, A. Bampouli, E. Brozzi, G. D. Stefanidis, M. Dusselier, T. Van Gerven and S. Kuhn, *Chem. Soc. Rev.*, 2025, **54**, 85–115.
- 5 C. Holland and R. Apfel, *IEEE Trans. Ultrason. Ferroelectr. Freq. Control*, 1989, **36**, 204–208.
- 6 O. Hamdaoui and K. Kerboua, *Energy Aspects of Acoustic Cavitation and Sonochemistry*, Elsevier, 2022.



7 P. R. Gogate, V. S. Sutkar and A. B. Pandit, *Chem. Eng. J.*, 2011, **166**, 1066–1082.

8 D. Meroni, R. Djellabi, M. Ashokkumar, C. L. Bianchi and D. C. Boffito, *Chem. Rev.*, 2022, **122**, 3219–3258.

9 A. Barchouchi, S. Molina-Boisseau, N. Gondrexon and S. Baup, *Ultrason. Sonochem.*, 2021, **72**, 105407.

10 T. Inui and M. Kang, *Appl. Catal., A*, 1997, **164**, 211–223.

11 J. Park, B. C. Kim, S. S. Park and H. C. Park, *J. Mater. Sci. Lett.*, 2001, **20**, 531–533.

12 Ö. Andaç, M. Tatller, A. Sirkecioğlu, I. Ece and A. Erdem-Şenatalar, *Microporous Mesoporous Mater.*, 2005, **79**, 225–233.

13 S. S. Bukhari, J. Behin, H. Kazemian and S. Rohani, *Fuel*, 2015, **140**, 250–266.

14 M. Yoldi, E. Fuentes-Ordoñez, S. Korili and A. Gil, *Microporous Mesoporous Mater.*, 2019, **287**, 183–191.

15 C. Belviso, *Ultrason. Sonochem.*, 2018, **43**, 9–14.

16 S. Lin, X. Jiang, Y. Zhao and J. Yan, *Sci. Total Environ.*, 2022, **851**, 158182.

17 C. T. Chen, K. Iyoki, Y. Yonezawa, T. Okubo and T. Wakihara, *J. Phys. Chem. C*, 2020, **124**, 11516–11524.

18 R. M. Dewes, H. Ramirez, M. Valdez, L. Pereira and T. V. Gerven, *Ultrason. Sonochem.*, 2022, **82**, 105909.

19 W. N. Nzodom Djozing, S. Valange, S. I. Nikitenko and T. Chave, *Dalton Trans.*, 2024, 16407–16421.

20 P. Pal, J. K. Das, N. Das and S. Bandyopadhyay, *Ultrason. Sonochem.*, 2013, **20**, 314–321.

21 H. Gürbüz, B. Tokay and A. Erdem-Şenatalar, *Ultrason. Sonochem.*, 2012, **19**, 1108–1113.

22 H. Ramirez Mendoza, J. Jordens, M. V. L. Pereira, C. Lutz and T. Van Gerven, *Ultrason. Sonochem.*, 2020, **64**, 105010.

23 A. Tadjarodi, M. Dehghani and M. Imani, *Appl. Organomet. Chem.*, 2018, **32**, 1–10.

24 M. Ashokkumar, *Ultrason. Sonochem.*, 2011, **18**, 864–872.

25 T. Sano, M. Itakura and M. Sadakane, *J. Jpn. Pet. Inst.*, 2013, **56**, 183–197.

26 D. V. Bruter, V. S. Pavlov and I. I. Ivanova, *Pet. Chem.*, 2021, **61**, 251–275.

27 Z. Liu, A. Chokkalingam, S. Miyagi, M. Yoshioka, T. Ishikawa, H. Yamada, K. Ohara, N. Tsunoji, Y. Naraki, T. Sano, T. Okubo and T. Wakihara, *Phys. Chem. Chem. Phys.*, 2022, **24**, 4136–4146.

28 J. Devos, M. A. Shah and M. Dusselier, *RSC Adv.*, 2021, **11**, 26188–26210.

29 S. Goel, S. I. Zones and E. Iglesia, *Chem. Mater.*, 2015, **27**, 2056–2066.

30 W. Qin, R. Jain, F. C. Robles Hernández and J. D. Rimer, *Chem. – Eur. J.*, 2019, **25**, 5893–5898.

31 Y. Lu, F. Qin, Y. Wang, R. Simancas, Y. Cai, J. N. Kondo, H. Gies and T. Yokoi, *Chem. Lett.*, 2024, **53**, upae010.

32 D. Schwalbe-koda, Z. Jensen, E. Olivetti and R. Gómez-bombarelli, *Nat. Mater.*, 2019, **18**, 1177–1181.

33 M. J. Mendoza-Castro, Z. Qie, X. Fan, N. Linares and J. García-Martínez, *Nat. Commun.*, 2023, **14**, 1–9.

34 J. Devos, S. Robijns, C. Van Goethem, I. Khalil and M. Dusselier, *Chem. Mater.*, 2021, **33**, 2516–2531.

35 R. Ageba, Y. Kadota, T. Maeda, N. Takiguchi, T. Morita, M. Ishikawa, P. Bornmann and T. Hemsel, *J. Korean Phys. Soc.*, 2010, **57**, 918–923.

36 M. Ishikawa, Y. Kadota, N. Takiguchi, H. Hosaka and T. Morita, *Jpn. J. Appl. Phys.*, 2008, **47**, 7673.

37 C. Aymonier, M. Bottreau, B. Berdeu and F. Cansell, *Ind. Eng. Chem. Res.*, 2000, **39**, 4734–4740.

38 P. E. Meskin, V. K. Ivanov, A. E. Barantchikov, B. R. Churagulov and Y. D. Tretyakov, *Ultrason. Sonochem.*, 2006, **13**, 47–53.

39 C. Cau, Y. Guarí, T. Chave, J. Larionova, P. Pochon and S. I. Nikitenko, *J. Phys. Chem. C*, 2013, **117**, 22827–22833.

40 Z. Liu, J. Zhu, T. Wakihara and T. Okubo, *Inorg. Chem. Front.*, 2019, **6**, 14–31.

41 S. I. Nikitenko, M. Brau and R. Pflieger, *Ultrason. Sonochem.*, 2020, **67**, 105189.

42 Z. Liu, T. Wakihara, D. Nishioka, K. Oshima, T. Takewaki and T. Okubo, *Chem. Commun.*, 2014, **50**, 2526–2528.

43 Z. Liu, T. Wakihara, D. Nishioka, K. Oshima, T. Takewaki and T. Okubo, *Chem. Mater.*, 2014, **26**, 2327–2331.

44 A. Javdani, G. Ivanushkin, A. Deneyer and M. Dusselier, *React. Chem. Eng.*, 2024, 379–391.

45 G. Ivanushkin and M. Dusselier, *Chem. Mater.*, 2023, **35**, 5049–5058.

46 C. Delacour, D. S. Stephens, C. Lutz, R. Mettin and S. Kuhn, *Org. Process Res. Dev.*, 2020, **24**, 2085–2093.

47 J. C. Crislip, J. Vicens, T. Pham, Y. Zhang, G. Tompsett and A. R. Teixeira, *J. Flow Chem.*, 2022, **12**, 397–408.

48 G. Feng, P. Cheng, W. Yan, M. Boronat, X. Li, J.-H. Su, J. Wang, Y. Li, A. Corma, R. Xu and J. Yu, *Science*, 2016, **351**, 1188–1191.

49 P. Cheng, G. Feng, C. Sun, W. Xu, J.-H. Su, W. Yan and J. Yu, *Inorg. Chem. Front.*, 2018, **5**, 2106–2110.

50 Y. Iida, K. Yasui, T. Tuziuti and M. Sivakumar, *Microchem. J.*, 2005, **80**, 159–164.

51 T. J. Mason, J. P. Lorimer, D. M. Bates and Y. Zhao, *Ultrason. Sonochem.*, 1994, **1**, 2–6.

52 D. B. Rajamma, S. Anandan, N. S. M. Yusof, B. G. Pollet and M. Ashokkumar, *Ultrason. Sonochem.*, 2021, **72**, 105413.

53 J. C. Barreto, G. S. Smith, N. H. Strobel, P. A. McQuillin and T. A. Miller, *Life Sci.*, 1994, **56**, 89–96.

54 T. Charbouillot, M. Brigante, G. Mailhot, P. R. Maddigapu, C. Minero and D. Vione, *J. Photochem. Photobiol., A*, 2011, **222**, 70–76.

55 S. Kanazawa, T. Furuki, T. Nakaji, S. Akamine and R. Ichiki, *J. Phys.: Conf. Ser.*, 2013, **418**, 012102.

56 X. Fang, G. Mark and C. Von Sonntag, *Ultrason. Sonochem.*, 1996, **3**, 57–63.

57 A. A. Atchley, *J. Acoust. Soc. Am.*, 1989, **85**, 152–157.

58 G. Bonilla, I. Díaz, M. Tsapatsis, H.-K. Jeong, Y. Lee and D. G. Vlachos, *Chem. Mater.*, 2004, **16**, 5697–5705.

